



FERMILAB-Conf-77/100-EXP
2500.000

A FINE GRAIN FLASH CHAMBER CALORIMETER^{*}

F. E. Taylor
Physics Department, Northern Illinois University
DeKalb, Illinois 60115

and

T. Ohsugi and J. K. Walker
Fermi National Accelerator Laboratory
Batavia, Illinois 60510

and

D. Buchholz and D. Miller
Physics Department, Northwestern University
Evanston, Illinois 60201

October 1977

^{*} Submitted to the IEEE Nuclear Science Symposium, San Francisco,
October 19-21, 1977



spark chamber gas (90% Ne + 10% He) which is allowed to continuously flow through the chamber at a rate of 1 to 2% of the chamber volume per minute. Transparent gas manifolds made from thermo-vacuum-formed Uvac plastic are glued to the ends of the polypropylene sheets to form a gas tight chamber. Aluminum plates glued to the polypropylene sheets serve as electrodes for the pulsed electric field. No special precautions seem to be needed in the assembly of a flash chamber. We have achieved good results without cleaning the polypropylene. Epoxy glue or two-component RTV, serves as a bonding agent. In Fig. 2 are shown the details of the construction of one flash chamber plane.

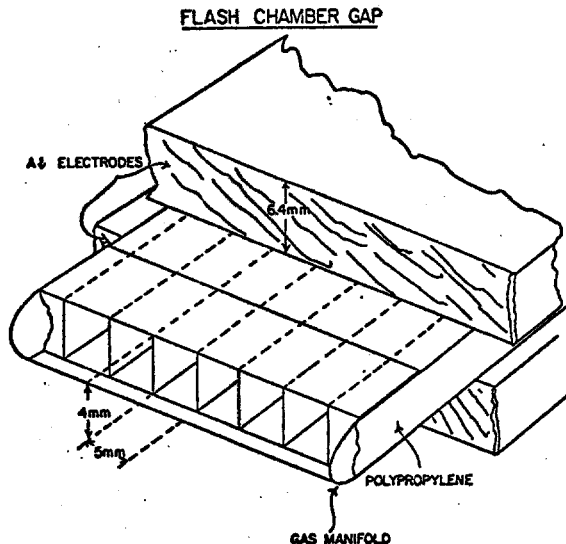


Figure 2. The construction of one flash chamber gap.

Calorimeter

The test calorimeter consists of 126-4 mm polypropylene planes 46 cm x 46 cm wide sandwiched between 6.4 mm sheets of aluminum. Every other polypropylene plane is fitted with a gas manifold (of the design shown in Fig. 2) to make a total of 63 flash chamber planes. The total number of active flash chamber cells in the calorimeter is 5,800. Figure 3 shows an elevation view of the calorimeter. Only one view of the tracks in the calorimeter was photographed. A 6 mm sheet of lead and a 6.4 mm thick scintillation counter are located every 20 cm in the calorimeter. The overall length of the calorimeter is roughly 1.5 meters.

The calorimeter consists of 16 radiation lengths and 3.5 collision lengths. The average radiation length in the calorimeter is 9.5 cm and the average collision length is 43.4 cm. Particle showers are sampled on the average every 25% of a radiation length and every 6% of a collision length. The shower sampling by the aluminum plates alone (within one module of 9-see Fig. 3) is every 14% of X_0 and every 5% of λ_0 . The average density of the calorimeter was 1.7 g/cm^3 .

FLASH CHAMBER CALORIMETER

15 X_0 , 3.5 λ_0 , 63 Chambers λ_0 Sampling = 5.6% of λ_0

X_0 Sampling = 24% of X_0

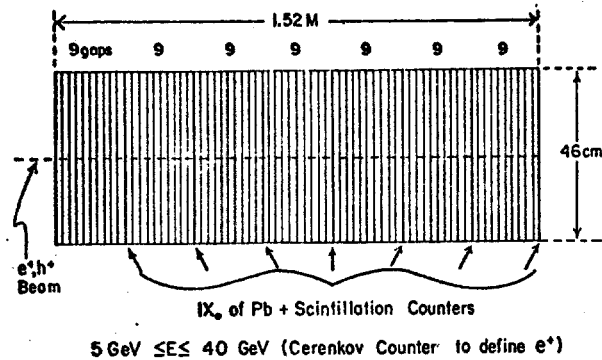


Figure 3. Schematic diagram of the flash chamber calorimeter.

Electrical Characteristics

The main electrical characteristics of the flash chambers are: 1) each flash chamber cell is electrically insulated from each other cell, and 2) there is no D.C. path of the stored energy of the triggered HV pulse through the chamber to ground. In other words, the region where the glow discharge takes place is insulated from the HV electrodes. Hence the flash chamber is capable of detecting many tracks in a given event since there is little energy "robbing".

The glow discharge, which propagates and fills the cell traversed by the particle, is initiated by a triggered HV pulse (typically 9 kV and 75 nsec. duration). This HV pulse is applied across the 4 mm dimension of the polypropylene sheets and is generated by a conventional spark gap-capacitor discharge circuit.

We have experimented with various time constants of the HV pulse. We find the best chamber operation is achieved for $\tau \sim 100 \text{ nsec}$. For time constants longer than 200 nanoseconds, adjacent cells begin to fire, spoiling the angular and energy resolution of the calorimeter.

In Fig. 4 we have plotted a typical HV plateau curve for a flash chamber in the test calorimeter. These data were taken by using 10 GeV muons supplied by the M5 test beam at Fermilab. The event rate was determined by the camera film transport which allowed only 1 trigger every beam spill, hence 1 event every 15 seconds. We see that the chamber plateaus at roughly 8 kV ($E \sim 20 \text{ kV/cm}$) at an 80% single track efficiency. We expect the multitrack efficiency to be essentially the same as the single track efficiency since there is little energy robbing. We have observed tracks with good efficiency up to 80° to the normal.

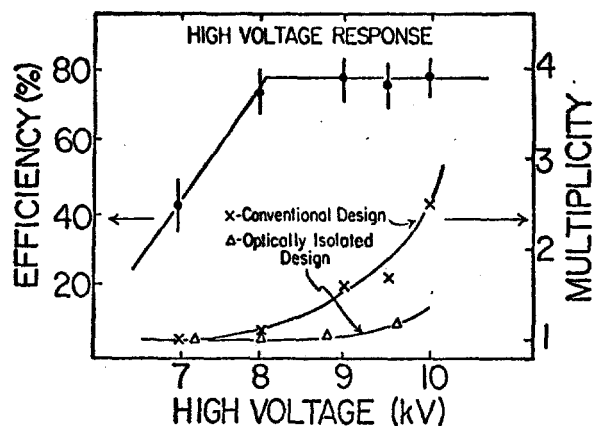


Figure 4. A typical HV plateau curve for a flash chamber in the test calorimeter is shown. The multiplicities of the number of firing cells given that one cell has fired for the two chamber designs are shown at the bottom of the figure.

We have studied the multiplicity of cells which fire given that one cell has fired. This multiplicity is plotted below the plateau curve in Fig. 4. We see that the cell multiplicity grows with increasing HV and becomes ~ 2 at 9.5 kV. This effect is somewhat troublesome since it tends to spoil the track resolution and the energy resolution of the calorimeter. The firing of adjacent cells is due either to UV light or the plasma of the glow discharge leaking from one cell to its adjacent cells. Hence we have built a gas manifold which provides better isolation between cells. This isolation is accomplished by gluing the transparent plastic end caps directly on the ends of the polypropylene sheets and by feeding the Ne and He gas in through holes in each cell with another gas manifold. The multiplicity versus HV for this new design is shown in the lower portion of Fig. 4. We see considerable improvement.

We have measured the flash chamber sensitivity time by inserting delay in the trigger pulse to the master spark gap. In Fig. 5, we have plotted the chamber efficiency as a function of this delay. We see that the chamber efficiency drops roughly linearly by $\sim 20\%$ out to ~ 1 μ sec delay. In addition we have found that the sensitive time is a function of the Ne + He gas flow rate. In the data of Fig. 5, the flow rate was 1.5% of the chamber gas volume/min. We have experimented with other flow rates and find that shorter sensitive times can be achieved by reducing the gas flow rate. The chamber recovery time after pulsing is ~ 100 msec. However no clearing field was used which can shorten this time.³

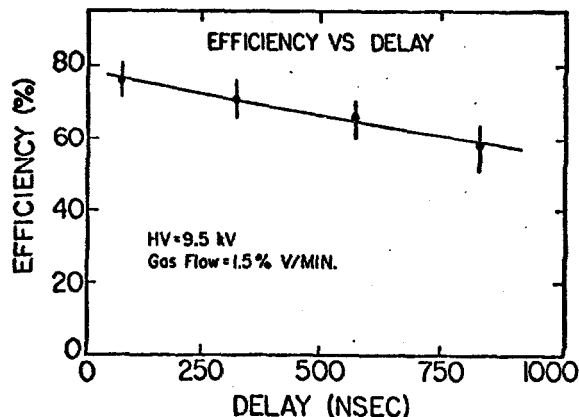


Figure 5. The flash chamber efficiency versus delay of the HV pulse is shown.

Read-Out

The glow discharges in the flash chamber can be easily photographed or detected by a vidicon or CCD. For the measurements reported here, we have used an 80 mm - f2.8 lens with 35 mm Eastman Kodak S0143 film. The film has an ASA rating of 500. We have digitized this film through the Film Analysis Facility at Fermilab.

Other read-out possibilities exist. We have verified the observation of Conversi, et al. that a small probe placed a short distance inside a flash chamber cell gives roughly a 100V pulse into 1 k Ω . We are investigating several schemes for reading these pulses out.

PERFORMANCE

The response of the test calorimeter to electrons (really positrons) and positive hadrons has been measured in the energy range of 5 to 40 GeV in the Meson Lab test beam at Fermilab. The test beam was equipped with an 18 m long gas Cerenkov counter which provided a clean trigger for electrons. The test beam contained roughly 80% π^+ , 20% p and $< 3\%$ e^+ .

Electrons

A set of typical electromagnetic showers at various energies is shown in Fig. 6. The incident electron enters from the left. We observe that the flash chambers are capable of supporting many tracks with no noticeable degradation of efficiency. The large multiplicity of cells after the first lead plate ($1X_0$) is clearly seen.

ELECTRON SHOWERS

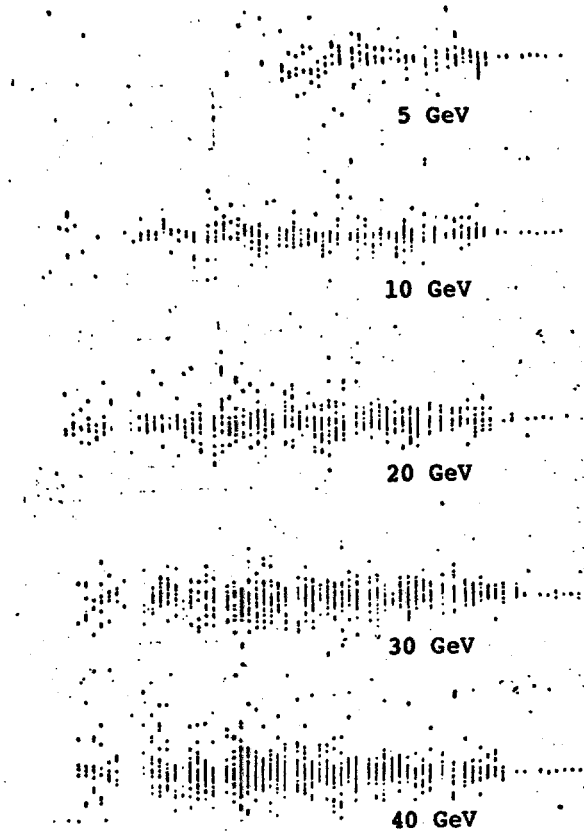


Figure 6. A set of typical electromagnetic showers at various energies is shown.

The number of cells which fire at a given shower depth for various incident energies is shown in Fig. 7. This figure shows the increase of the number of cells

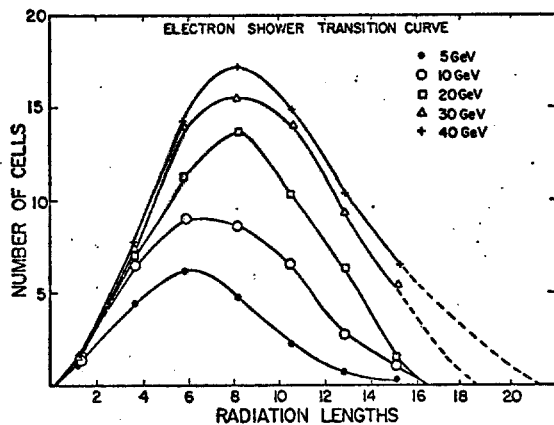


Figure 7. The average number of cells which fire at a given shower depth for several incident electron energies.

with increasing incident energy as well as the expected slow increase in the depth of the shower maximum. In Fig. 8 we show

the lateral distributions for 10 and 30 GeV electromagnetic showers as a function of shower depth. We see that for energies < 30 GeV electron showers in our calorimeter are contained in a cylinder of roughly < 20 cm diameter.

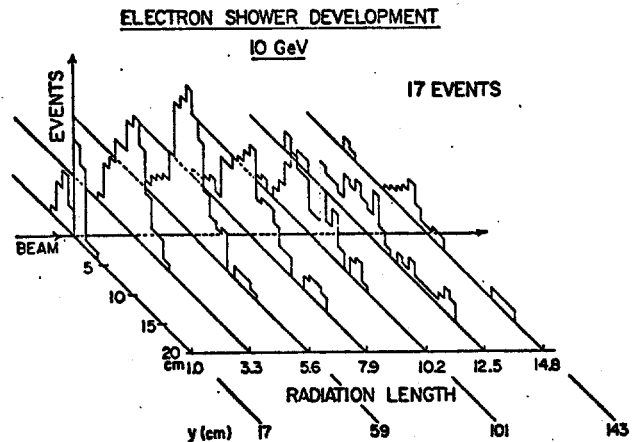


Figure 8a

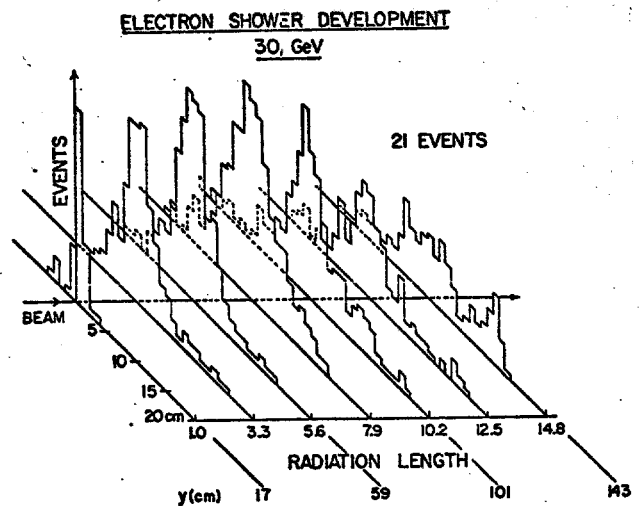


Figure 8b

Figure 8 a) The lateral distributions of 10 GeV electromagnetic showers at various shower depths. b) The lateral distributions of 30 GeV electromagnetic showers versus shower depth.

The average of the total number of firing cells versus the energy of the incident electron is shown in Fig. 9. At 30 and 40 GeV we have corrected for the small shower leakage (< 10%) out the back of the calorimeter. We find the electron energy response to be roughly linear up to 20 GeV. But for electron energies above 20 GeV the number of electron-positron pairs at the shower maximum is too large to distinguish individual particles with the cell size of 4 mm x 5 mm, and thus the energy response of the calorimeter becomes nonlinear. Even with this nonlinear energy response above 20 GeV, useful energy measurements may be made up to 40 GeV.

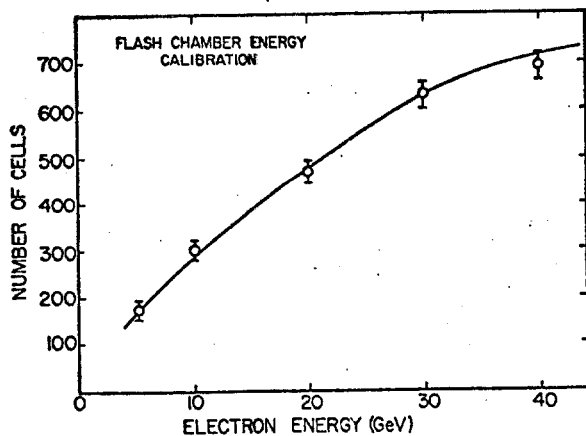


Figure 9. The average number of firing cells versus the energy of the incident electron.

Electron Energy Resolution

We next direct our attention to the electron energy resolution of the calorimeter. In Fig. 10 we show a histogram of the number of cells which fire for incident electrons of 20 GeV. A gaussian adequately describes the data with $\sigma/\text{mean} \approx 5.5\%$. The electron energy resolution is then computed by accounting for the nonlinear energy response shown in Fig. 9.

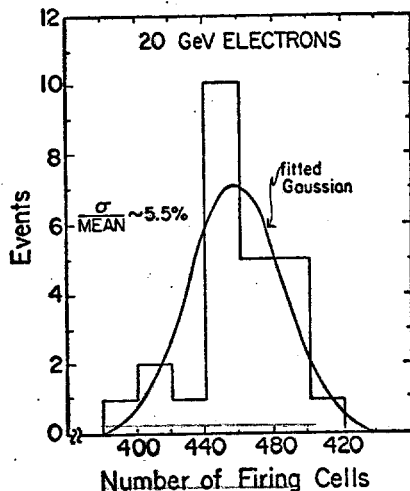


Figure 10. Histogram of the number of cells which fire for 20 GeV electrons.

The energy resolution versus the incident electron energy is shown in Fig. 11. We see that the energy resolution is roughly constant and is given by $\sigma(E)/E \approx \pm 10\%$ for $5 \leq E_e \leq 40$ GeV.

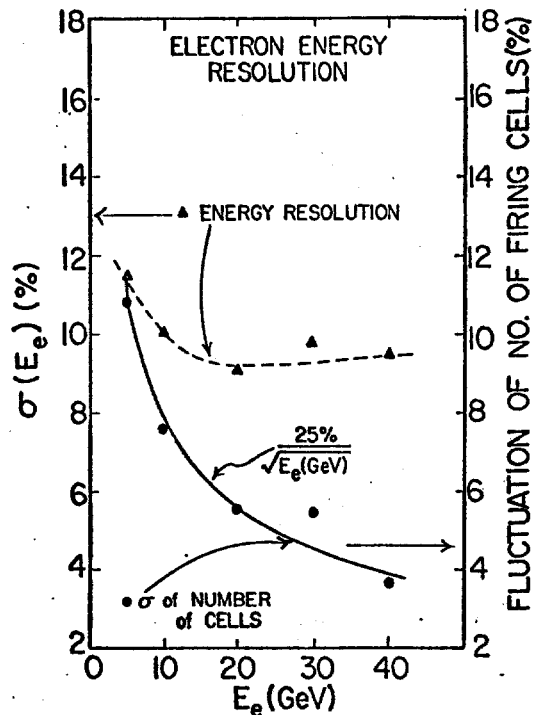


Figure 11. The energy resolution σ/mean in percent versus the incident electron energy (left hand scale). The corresponding fluctuations of the number of firing cells in percent are shown on the right hand scale.

Electron Angular Resolution

The electron angular resolution of the calorimeter has been determined by digitizing the x-y coordinates of every firing cell in a sample of electromagnetic shower events. (x is perpendicular to the incident electron direction, y is parallel to this direction.) From these coordinates we have computed the lateral position (x) of the center of gravity of the firing cells for a given shower depth (y). In Fig. 12a we show the center of gravity coordinates of a typical 30 GeV electromagnetic shower. (The x-y coordinates in Fig. 12 are in arbitrary units.) The central axis of the shower is quite evident, but we notice a considerable scattering of the center of gravity positions about the central axis due to the statistical nature of the shower.

Careful treatment of these shower fluctuations is necessary to obtain good angular resolution. Hence we have adopted a two pass fitting procedure to determine the shower direction. In the first pass, a straight line is fitted to the center of gravity of the data by assigning equal weights to each center of gravity coordinate. The first pass fit is shown by the solid line in Fig. 12a. The first pass fit is then used to define a "road" to

cut out data which show large fluctuations about the first pass line. This road is made narrow at the front end of the shower and linearly broadens as the beam direction coordinate (y) is increased. The space between the dashed lines in Fig. 12a is the road. This recipe accounts for the expected increase in the lateral fluctuations of the shower as the shower depth is increased but eliminates spurious fluctuations. Typically $< 10\%$ of the coordinate data for a given event are eliminated by this cut. The surviving data are then refit, but this time the coordinates at the beginning of the shower are weighted more heavily than the coordinates at the end of the shower. This differential weighting is performed by allowing the uncertainty of each center of gravity coordinate to increase linearly with increasing y . This second pass fit of the event of Fig. 12a is shown in Fig. 12b.

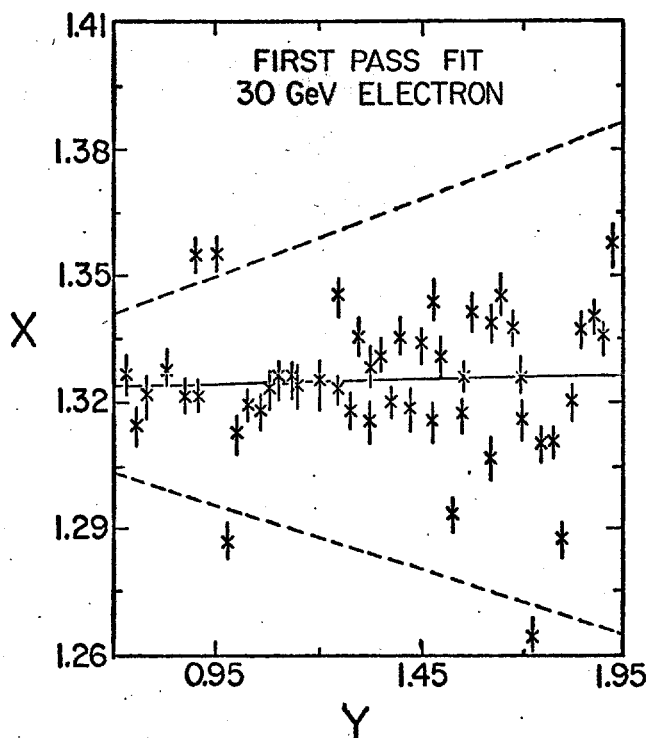


Figure 12a

Figure 12. An example of the two pass fitting procedure of a 30 GeV electromagnetic shower. The lateral center of gravity coordinates x are plotted against the shower depth y . a) The first pass fit to the shower is denoted by the solid line. The space between dotted lines is the "road". b) The second pass fit is shown. Note the increase of the error flags as the shower depth y is increased.

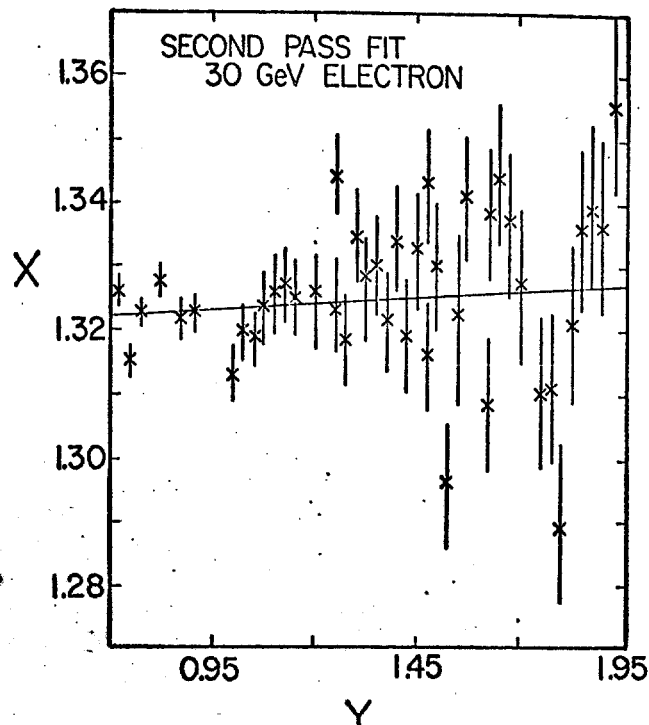


Figure 12b

The resulting electron projected angle resolution determined by this two pass fitting procedure for $5 \leq E \leq 30$ GeV is shown in Fig. 13. We see that the electron angular resolution decreases with increasing energy and can be described over the range of our measurement by $\sigma(E_e) = (2 + 70/E_e)$ (GeV) mrad. For comparison, we show in Fig. 13 the angular resolution for 10 GeV muons. The data suggest that in the high energy limit, the angular resolution of electrons approaches that of muons.

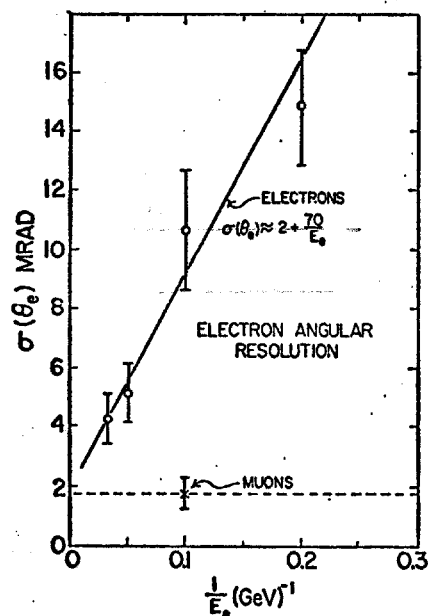


Figure 13. Projected (1 view) electron angle resolution versus the reciprocal of the electron energy. The angle resolution for 10 GeV muons is shown for comparison.

In Fig. 14 we show the electromagnetic shower angular resolution versus the shower sampling interval. We see that the angular resolution of a 10 GeV electron is degraded by roughly a factor of 2 when the sampling interval is increased from $0.25 \lambda_0$ to $1.0 \lambda_0$. The resolution degradation for 30 GeV showers on the other hand is less severe. Hence to obtain good angular resolution at low energies, it is important to have a fine-grain sampling of the shower.

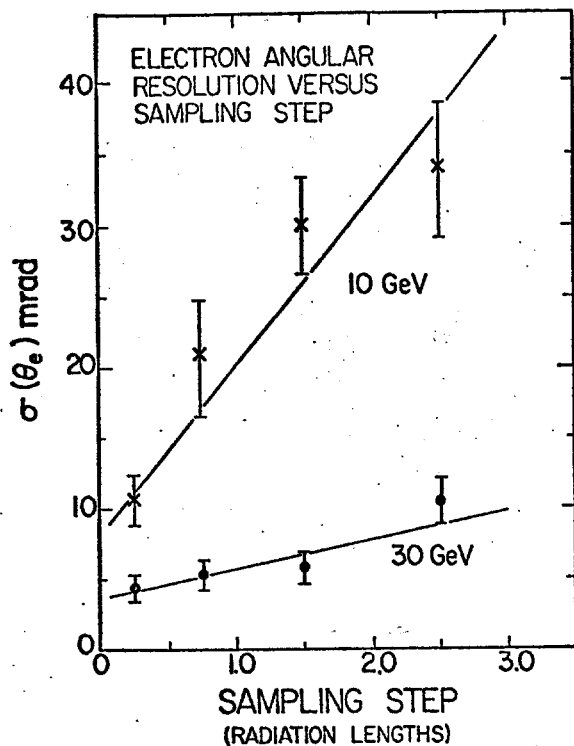


Figure 14. Electron angular resolution versus the shower sampling step for 10 GeV showers and 30 GeV showers.

Hadrons

Hadron showers have been measured in the energy range 5 to 40 GeV. Due to the small number of collision lengths ($3.5 \lambda_0$) in the test array, the hadron shower could not be fully contained. However we have determined the most important feature of the hadron response in the study of neutral current weak interactions, namely energy flow direction resolution of the calorimeter.

Electron/Hadron Rejection

In Fig. 15 we show three typical hadron showers at 20 and 30 GeV. We see that hadron showers are readily distinguishable from electron showers shown in Fig. 6 because of the larger average p_{\perp} in a hadron collision and the slower shower development curve of the hadron showers.

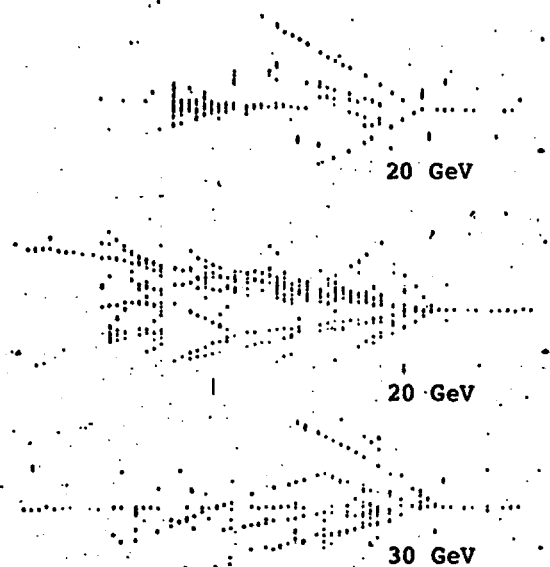


Figure 15. Three typical hadronic showers are shown.

We have checked this electron/hadron discrimination by taking data with no selection on the incident particle type and attempting to identify electrons in the data. A simple criterion was used to identify hadrons. If an event downstream of two radiation lengths contained at least one track, defined as at least nine cells forming a line without adjacent firing cells, then the incident particle was called a hadron. Otherwise it was identified as an electron. These measured electron/hadron (e/h) ratios for various incident energies were compared with the measured e/h ratios determined by the gas Cerenkov counter. The e/h ratios determined by the flash chamber detector and the Cerenkov counter were consistent with each other. We conclude that hadron rejection using this criterion is at least 100:1 at 30 and 40 GeV.

The lateral distributions of hadron cascades for 10 GeV and 40 GeV are shown in Fig. 16. In these figures the data are shown, for clarity, only every ninth detecting plane ($0.50 \lambda_0$). We see that the lateral spread of hadronic showers is greater than that of electromagnetic showers. For example a 40 GeV hadron shower is contained in a cylinder of ~30 cm diameter (less than the lateral size of the calorimeter), whereas an electron shower of this energy requires only ~20 cm for containment. Comparison of Fig. 16 with Fig. 8 shows that the longitudinal development of hadron showers after the first hadron interaction appears to be quite similar to electromagnetic shower development. Hence a trigger which discriminates between hadrons and electrons must be sensitive to the lateral spread of the shower.

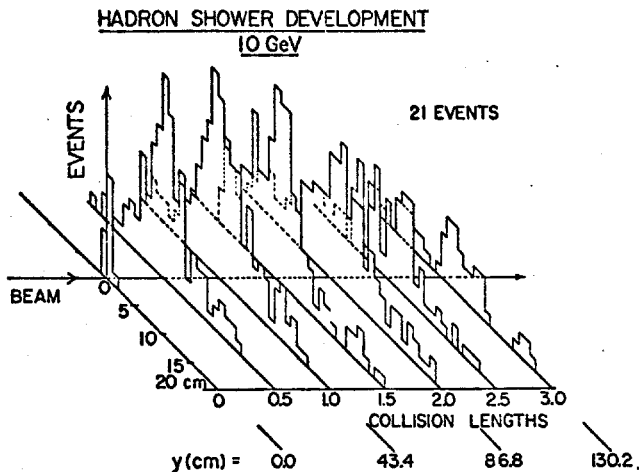


Figure 16a

Figure 16. The lateral distribution of hadronic cascades versus shower depth. a) 10 GeV incident hadrons and b) 40 GeV incident hadrons.

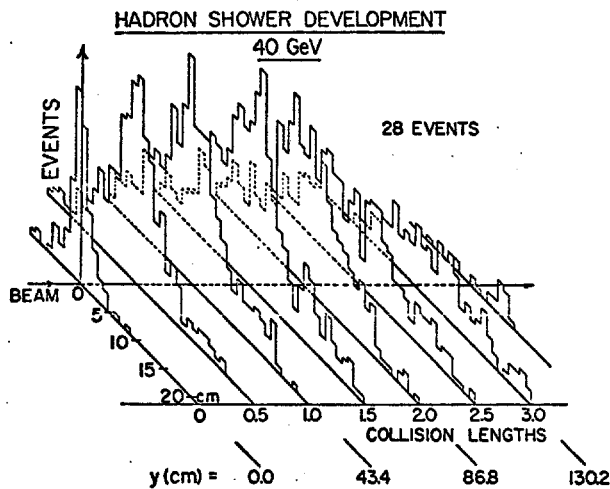


Figure 16b

Hadron Energy Flow Angle Resolution

We have used the first interaction of hadronic cascades to simulate the hadrons produced in neutrino interactions. The hadron energy flow direction of the particles emerging from this interaction point is determined by a least squares fit to the primary vertex position and the center of gravity coordinates of the hadron cascade versus shower depth. Since our calorimeter was only 3.5 interaction lengths long, we have only analyzed hadron showers which have interacted in the first 9 plates of the calorimeter. We have used the same two pass procedure as was used for electrons, but in this case we have made the road much broader at the back of the calorimeter and have increased the errors associated with each center of gravity coordinate to be 4 times larger than in the case of electromagnetic showers. This was necessary since the shower fluctuations are considerably larger in hadron showers than in electromagnetic showers. In Fig. 17 we show the energy flow angle resolution versus $1/E_H$. We see that the angle resolution becomes better with increasing energy

as in the case of electromagnetic showers and has an energy dependence of roughly $\sigma(\theta_H) = 11 + 230/E_H$ over the range of our measurements. As in the case of electromagnetic showers, we find that fine-grain sampling of the hadronic cascade is important to achieve good angular resolution. For example, when 20 GeV hadronic cascades are sampled every 66% of a collision length rather than every 5.6% of λ_0 , the angular resolution is $\sigma \approx 46$ mrad rather than $\sigma \approx 25$ mrad. We are in the course of extending these measurements to higher energies $E_H \leq 300$ GeV.

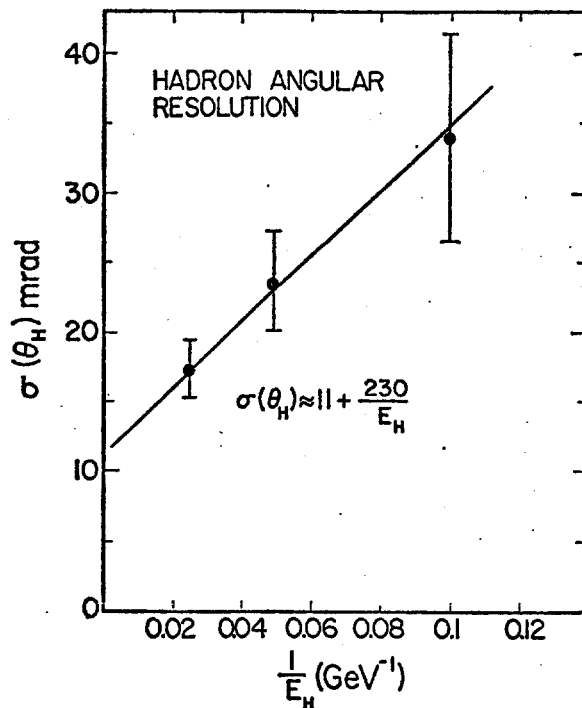


Figure 17. The hadron energy flow angle resolution is plotted against the reciprocal of the incident hadron energy.

CONCLUSIONS

A flash chamber calorimeter is inexpensive, easy to construct and operate and hence is suitable for use in a large system. Good angle resolution, energy determination, and excellent electron-hadron determination are all obtainable with such a calorimeter. These characteristics make flash chamber calorimeters attractive instruments for the next generation of neutrino detectors and possibly for colliding beam detectors.

ACKNOWLEDGEMENTS

We would like to thank D. Burandt for his technical support and the Film Analysis Facility, especially, D. Bogert, R. Hanft, and J. Wolfson for their help in digitizing the film. W. Muller is thanked for his help in the data collection and reduction. We are indebted to C. Kerns for help in building the spark gap system.

REFERENCES

¹M. Conversi, et al.; "A Low-Cost Electrically Pulsed Shower Detector" EP Internal Report 76-20 CERN, 26 Sept. 1976. M. Conversi, et al., "Flash Chambers of Plastic Material", 15 Aug. 1977 submitted to Nuclear Instruments and Methods.

²One supplier of the polypropylene is:
Primax Plastic Corporation
1 Raritan Road
P. O. Box 520
Oakland, New Jersey 07436

³M. Conversi and collaborators discuss an AC clearing field operating at 50 Hz. See Ref. 1, and references therein.

⁴F. Ceradini, et al., "A Low-Cost Total Absorption Track Detector of High-Energy Particles", 15 Aug. 1977. Submitted to Nuclear Instruments and Methods.

⁵Streamer chamber tracks have been recorded with CCD's. Presumably flash chambers give comparable light output. See F. Villa and L. C. Wang; SLAC-Pub-1890 (March 1977)

